



Arab American University-Palestine

Faculty of Graduate Studies

**Copper doping effects on the optical properties of InSe
thin films**

By

Fatima Mohammed Aboalrub

Supervisor

Prof. Atef Qasrawi

**This thesis was submitted in partial fulfillment of the
requirements for The Master's degree in Physics**

September/2019

© Arab American University –2019. All rights reserved.

Copper doping effects on the optical properties of InSe thin films

By

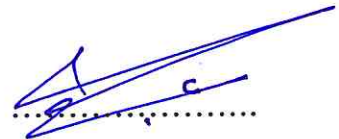
Fatima Mohammed Aboalrub

This thesis was defended successfully on September 21st 2019 and approved by:

Committee members

Signature

1. Prof. Dr. Atef Fayez Qasrawi (Supervisor)



2. Dr. Hazem Khanfar (Internal Examiner)



3. Prof. Dr. Mohameed Elsaid (External Examiner)



Declaration

The work in this thesis, unless otherwise referenced, is the researcher's own work and has not been submitted elsewhere for any other degree or qualification.

Student's Name: Fatima Mohammed Ismael Abo AlRub

Signature: 

Date 21/10/2019

Dedication

To My Family

Acknowledgments

I thank all who in one way or another contributed in the completion of this thesis. My first and greatest thanks are to Allah. He above all was, is, and will be the source of help and guidance that counts. His help kept us going through many frustrations and His guidance brought us back on track when our frustrations tended to drive us astray.

Starting with endless thanks for my supervisor Prof. Dr. Atef Fayez Qasrawi. Who didn't hold back any efforts for his patience, continuous support, compassionate treatment, encouragement my research and for allowing me to grow as a research scientist. His advice on my research has been invaluable. His critical comments and correction were important to the completion of this work and has taught me unnumbered lessons on the academic research workings. He encouraged me to prove myself, think independently and to polish my personality to be ready to discuss the thesis I work on. A lot of talk is said, but none of them can describe my gratitude to Dr. Atef Qasrawi, in short, without his help this thesis would not have been finished today.

My genuine thanks to all department members: Prof. Dr. Zaki Saleh, Dr. Adli Saleh, Dr. Muayad Abu Saa, Dr. Ahmad Omar, Prof. Mohammad Abu Samra, Dr. Soliman Rabaa, and Mr. Anan Hussien.

With great appreciation I shall acknowledge my colleague Olfat Omareya. Your scientific tips, your friendly advice, your soothing words and your big heart helped me face all the obstacles and continue with my work. I will never forget your kindness. I cannot forget all

friends who went together through hard times, cheered me up, and celebrated each achievement

I have to thank the most important of those who have the credit to be here today. I owe a special thanks to my family, my mom and dad, my brother, my sister, who supported me and helped me throughout my life and during this study. I dedicate this work to you all. Mom, dad I do not know how to thank you enough for providing me with the opportunity to be where I am today. I love you so much.

I do not know how to begin with saying thank you to my soul mate, my dearest husband and my best friend Waleed I thank you for everything, for being so understanding and for putting up with me through the toughest moments of my life.

Abstract

In this thesis, we attempted to improve the optical and dielectric performance of InSe thin films through doping of copper into the structure of InSe. The InSe thin films which are prepared by the thermal evaporation technique under vacuum pressure of 10^{-5} mbar onto glass substrates were structurally and optically characterized by means of X-ray diffraction and optical spectrophotometry techniques. The doping content in the films was scanned by the energy dispersive spectroscopy technique. Undoped and Cu-doped InSe thin films with doping content of 1.5 at% and 3.0 at% were studied and analyzed. The EDX analyses has shown that while the formed films preferred the InSe monophase in the presence of Cu $\text{In}_{30}\text{Se}_{70}$ is preferred. It was observed that at this level of doping the amorphous nature of the films is not altered. However, the optical transitions which revealed energy band gap values of 1.38 eV for the undoped films is changed from indirect to direct type upon doping. The doping of 3.0 at% increased the value of energy band gap by 29% and decreased the width of the energy band in InSe by 76% indicating better optical performance. In addition, the doping with 1.5 % improves both of the dielectric and conduction properties. The dielectric constant at resonance energy increased from 12 to 15 and the drift mobility increased from 45 to 55 cm^2/Vs upon doping.

List of contents

	Title	Page No.
	List of tables	
	List of figures	
Chapter One	Introduction and Literature Survey	1
Chapter Two	Theoretical Background	4
	2.1 X-ray diffraction Technique	4
	2.2.1 Derivation of Tauc's equation	7
	2.2.2 Fresnel's equations	10
	2.3 Drude-Lorentz Model	13
	2.4 Interbands	17
Chapter Three	Experimental Details	19
	3.1 Substrate cleaning	19
	3.2 Preparation of Cu doped InSe thin films	19
	3.3 Thin Films Analysis	20
	3.4 X-ray diffraction	21
	3.5 Scanning Electron Microscopy(SEM)	22
	measurements	
	3.6 Energy-dispersive X-ray spectroscopy (EDX)	23
	3.7 Optical Measurements	23
Chapter Four	Results and Discussion	25
	4.1 Scanning electron microscope and compositional analysis	25
	4.2 Structural Analysis	27
	4.3 Optical Analysis	28
Chapter Five	Conclusions	42
	References	43
	المخلص	48

List of tables

No.	Title	Page No.
2.1	The 14 lattice types in three dimensions.	6
4.1	The fitting parameters of Drude-Lorentz model for InSe, doped InSe with 1.50 at% Cu and doped InSe with 3.00 at% Cu.	41

List of figures

No.	Caption	Page No.
2.1	Bragg's Law for X-ray diffraction	5
3.1	The 600 VCM evaporation system	20
3.2	Rikagu Miniflex 600 diffractometer	22
3.3	The scanning electron microscope device.	23
3.4	The UV-VIS spectrophotometer	24
4.1	The energy dispersive X-ray spectroscopy for (a) undoped and (b) 1.5 at. % doped and (c) 3.0 at. % copper doped indium selenide thin films.	26
4.2	XRD pattern of InSe, InSe doped with 1.50 at% Cu and InSe doped with 3.00 at% Cu thin films at room temperature	28
4.3	The transmittance spectra for InSe, InSe doped with 1.50 at% Cu and InSe doped with 3.00 at% Cu.	29
4.4	The reflectance spectra for InSe, InSe doped with 1.50 at% Cu and InSe doped with 3.00 at% Cu.	30
4.5	The relation between absorption coefficient (α) and the incident photon energy in (eV) for InSe, 1.50 % Cu doped InSe and 3.00% Cu doped InSe	31
4.6	The $\ln(\alpha)$ -E variation for InSe, doped InSe with 1.50 at% Cu and doped InSe with 3.00 at% Cu.	33
4.7	The $(\alpha E)^2$ - E variation for InSe, doped InSe with 1.50 at% Cu and doped InSe with 3.00 at% Cu.	35
4.8	The $(\alpha E)^{1/2}$ - E variation for InSe, doped InSe with 1.50 at% Cu and doped InSe with 3.00 at% Cu.	36
4.9	The real part of the dielectric constant.	37
4.10	The imaginary part of dielectric constants for InSe, doped InSe with 1.50 at% Cu and doped InSe with 3.00 at% Cu. The black colored lines are fitting of the Drude –Lorentz equation.	39

List of Symbols

Symbol	Acronym
InSe	Indium Selenide
Cu	Copper
Θ	Bragg angle
n	Integer
d	Inter-planar distance
λ	Wavelength
γ	The inverse of the electron scattering
λ	Wavelength
E_c	Conduction Band
E_v	Valance Band
t_c	Critical Thickness
a_s	Substrate Lattice constant
a_e	Epitaxial Layer Lattice Constant
Δ_a	The lattice mismatch
α	Absorption Coefficient
$\hbar\omega$	Photon Energy
$\rho(\hbar\omega)$	Density of Final States
\vec{A}	Vector Potential
P	The exponent of Tauc's equation
E_g	Energy band gap
k	Extinction coefficient
ϵ_{eff}	The effective dielectric constant
ϵ_{im}	The imaginary part of the dielectric constant
ϵ_r	The real part of the dielectric constant
m^*	The effective mass
μ	The drift mobility
r	Electron Position Vector
ψ_i, ψ_f	Wave Function of Initial and Final State
$P_{i \rightarrow f}$	Quantum Mechanical Transition Rate From Initial To Final State
U_i, U_f	Envelope Wave Function

Chapter One

Introduction and Literature Review

InSe thin films are one of the famous research materials as it plays role in many technological applications. The materials itself is photovoltaic and exhibit energy band gap of ~ 1.4 eV. It has been widely used in the fabrication of microwave sensors [1], as a multi-level switching phase change nano-pillar device [2] and as ultrathin and flexible optoelectronic device [3]. It was demonstrated that nano-layers of InSe photodetectors, designed on rigid SiO_2/Si substrate and on flexible polyethylene terephthalate (PET) films, are capable of conducting broadband photodetection from the visible to near-infrared region (450–785 nm) with photoresponsivities of 12.3 AW^{-1} at 450 nm (on SiO_2/Si) and 3.9 AW^{-1} at 633 nm (on PET) [3]. In addition, InSe is reported to follow the footsteps of graphine in displaying pronounced potential for the production of ultrathin optoelectronic devices [4].

Nanostructured InSe thin films are obtainable by the thermal evaporation technique under a vacuum pressure of 10^{-4} Pa [5]. They are also reported to be prepared by using metal-organic chemical-vapor deposition (MOCVD) [6] and by the electron beam evaporation techniques [7]. One of the most important troubles that the InSe nano-layer based devices suffers from is the amorphous nature of its as grown type, the very low density of free carrier concentration, the ability of the energy band gap tuning [8] and the surface roughness of the films. All these parameters lower the effectiveness of the InSe based devices. The carriers available for conduction in these devices are relatively low. Such property makes the current values low and lead to

high biasing voltages. These optoelectronic devices can then work in passive mode only. In addition, the energy band gap tuning helps in extending the absorption region of the InSe to wider range of visible and IR light spectrum. Several trails have been carried out to overcome these problems. As for example, quantum confinement on InSe nanosheets allowed tuning the energy band gap in the range of 1.20-1.47 eV [8], post annealing at 150-200 °C improved the crystalline and photovoltaic properties of the films [9], Doping with Gd, Ho and Dy highly affected the recombination centers in the InSe material [10], Cd doping alters the photoconductivity and lattice parameters of the hexagonal InSe thin films [11] and hydrogen implantation drastically lowered the energy band gap from 1.5 to 0.97 eV [12].

The copper ionic radius (Cu^{+3}) is 0.53 Å which is larger than that of Se (0.50 Å) and that of Indium (0.94 Å). The crystal structure of Cu is monoclinic while that of Se and indium are hexagonal and tetragonal, respectively. Thus, the doping of InSe with Cu which is studied here in this thesis for the first time is expected to derive a new features based on these structural types. It is expected to create new impurity level and alter the band structure of InSe. As supportive example, the optical absorption coefficient for thermally deposited and heat treated Cd-doped InSe films in the spectral range of 0.8 to 1.8 eV is affected by Cd impurities. For these samples, one observes a defect-induced tail at the lowest photon energies, a roughly exponential behavior of the absorption edge at intermediate energies, and a power law dependence at the highest energies [13].

In this thesis, we will discuss the Cu doping effects on the structural and optical properties of InSe. Light doping process will be actualized so that degeneracy effects are prevented. In the second chapter of this thesis, the theoretical background needed to easify the understanding of the results is mentioned and discussed. In the third chapter, the instruments used for carrying out the experiments are shown. The working principles of these units are also reported. In addition, the fourth chapter discusses the main results and the related discussions that explains the effect of copper doping on the properties of InSe. In the final chapter, the concluding remarks are reported.

Chapter Two

Theoretical Background

2.1 X-ray Diffraction Technique

X-ray diffraction (XRD) is a powerful technique for characterizing crystalline materials. It provides information about structures, phases, preferred crystal orientations, and structural parameters. For example, average grain size, crystallinity, strain, and crystal defects. X-ray diffraction peaks are produced by constructive interference of a monochromatic beam of X-rays scattered at specific angles from each set of lattice planes in a sample. The distribution of atoms determines the peak intensities within the lattice. As a result, the X-ray diffraction pattern is the imprint of periodic atomic arrangements in a material. The technique of X-ray diffraction pertaining to the fields of pharmaceuticals, forensic science, geological applications, microelectronics, and glass manufacturing, as well as in corrosion analysis [14].

X-ray diffraction technique is used to obtain structure of crystalline materials under various conditions like temperature, pressure, electric and magnetic field [15]. From the intensive peaks we determine positioning the unit cell dimensions. This process is called indexing. Miller indices (hkl) are necessary to be assigned for each peak to index [16].

Twisted layers resemble crystal lattices, which under certain circumstances are able to lead to a phenomenon known as Bragg's diffraction. This diffraction occurs when radiation having a wavelength comparable to successive crystallographic planes is scattered by different lattice planes that remain separated by the d interplanar distance. Therefore,

depending on the wavelength of the incident wave (λ), these scattered waves are able to interfere constructively according to the Bragg's law:

$$m\lambda = 2d\sin\theta \quad 2.1$$

Where λ wavelength in nm, d a lattice spacing in nm and m is a positive integer ($m = 1, 2, 3, \dots$) and θ is the scattering angle [17].

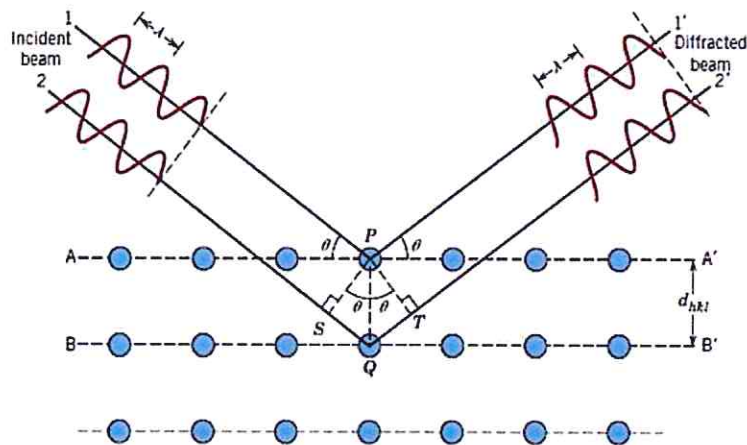


Fig. 2.1: Bragg's Law for X-ray diffraction [18].

Table 2.1 The 14 lattice types in three dimension [19].

System	Number of lattice	Restrictions on conventional cell axes and angles
Triclinic	1	$a_1 \neq a_2 \neq a_3$ $\alpha \neq \beta \neq \gamma$
Monoclinic	2	$a_1 \neq a_2 \neq a_3$ $\alpha = \gamma = 90^\circ \neq \beta$
Orthorhombic	4	$a_1 \neq a_2 \neq a_3$ $\alpha = \beta = \gamma = 90^\circ$
Tetragonal	2	$a_1 = a_2 \neq a_3$ $\alpha = \beta = \gamma = 90^\circ$
Cubic	3	$a_1 = a_2 = a_3$ $\alpha = \beta = \gamma = 90^\circ$
Trigonal	1	$a_1 = a_2 = a_3$ $\alpha = \beta = \gamma < 120^\circ \neq 90$
Hexagonal	1	$a_1 = a_2 \neq a_3$ $\alpha = \beta = 90^\circ$ $\gamma = 120^\circ$

The general lattice is triclinic, and there are 13 special lattices. These are grouped for convenience into systems classified according to seven types of cells as illustrated in table 2.1, which are triclinic, monoclinic, orthorhombic, tetragonal, cubic, hexagonal, and trigonal. The division into systems is expressed in table 2.1 in terms of the axial relations that describe the cell [19]. The X-ray diffraction patterns of an amorphous material such as a glass consists of broaden peaks, when viewed on the plane normal to the incident X-ray beam [19].

2.2.1 Derivation of Tauc's equation

The optical energy band gap and the predominant electron transition involved in the absorption process can be determined by the dependence of optical absorption coefficient on the incident photon energy. This relation is known as Tauc's equation [20]. The absorption coefficient spectra of the films were calculated with the help equation:

$$T = \frac{(1-R_{glass})(1-R_{film})e^{-\alpha d}}{(1-R_{glass}R_{film})e^{-2\alpha d}} \quad 2.2$$

Where d is the thickness of the sample. The optical absorption coefficient (α) is calculated using the relation [21].

$$\alpha = \frac{(\hbar\omega)(\text{transition probability/volume time})}{\text{total intensity}} \quad 2.3$$

$$\alpha = \frac{(\hbar\omega)(P_{i \rightarrow f})}{I} \quad 2.4$$

To solve the equation, we need an expression for $(P_{i \rightarrow f})$ and I . $(P_{i \rightarrow f})$ is quantum mechanical transition rates from initial to final state, defined by golden rule.

$$(P_{i \rightarrow f}) = \frac{2\pi}{\hbar} |M_{if}|^2 \rho(\hbar\omega) \quad 2.5$$

Where $\rho(\hbar\omega)$ is the density of final states and M_{if} is a matrix element describing the effect of external perturbation which couples the initial and final states defined as:

$$M_{if} = \frac{e}{m_o} \vec{A} \cdot \vec{p} \quad 2.6$$

With m_o the mass of free electrons, p the electron momentum defined as $\vec{p} = \hbar \vec{\nabla}$ and

A is the vector potential of the incident field and expressed as

$$A(r, t) = A_0 \exp(i(k \cdot r - \omega t)) \quad 2.7$$

Where A_0 is the initial potential at $t=0$, while the exponential is the Taylor expansion which is ignored when $A=A_0$ in the electric dipole approximation ($[k \cdot r]$ term is very small $\sim 10^{-3}$), so the interaction Hamiltonian simplifies to;

$$M_{if} \approx e_r \cdot \varepsilon_{\text{photon}} \quad 2.8$$

Where, r is the electron position vector measure from the center of mass of atom, e_r is the electron dipole moment (p_e), and $\varepsilon_{\text{photon}}$ is the amplitude of the light wave. According to the dipole approximation, the electric field of light waves is equal to [22]:

$$\varepsilon_{\text{photon}} = i\omega A_0 \quad 2.9$$

The interaction Hamiltonian and the wave functions of the initial (ψ_i) and final (ψ_f) states must be known in order to describe the perturbation of the system due to the light irradiance [23].

$$\psi_i(r) = \frac{1}{\sqrt{V}} u_i(r) e^{ik_i \cdot r} \quad 2.10(a)$$

$$\psi_f(r) = \frac{1}{\sqrt{V}} u_f(r) e^{ik_f \cdot r} \quad 2.10(b)$$

Where u_i and u_f are the envelope wave functions for the initials and final states, respectively, V is the volume normalization, and k_i and k_f are the wave vectors for the initial and final electron states, respectively. Substituting the wave functions and the perturbation Hamiltonian into the matrix element, we get

$$M_{if} = \frac{e}{V} \int u_f(r) e^{-ik_i r} (\varepsilon_{photon} \cdot e_r) u_i(r) e^{ik_i r} d^3r \quad 2.11$$

The electric dipole moment of the transition (M_{if}) caused by light is different for every material. With the interaction matrix solved, the remaining part of the quantum mechanical transition rate is $g(\hbar\omega)$. The density of states which is equal for a parabolic band is given by [24],

$$g(\hbar\omega) = \frac{1}{2\pi^2} \left(\frac{2m^*}{\hbar^2} \right)^{3/2} (\hbar\omega)^{1/2} \quad 2.12$$

Here ($\hbar\omega$) is the energy and m^* is the effective mass. The above equation evaluated at initial and final states to get the joint density of states. Assuming a term based on conservation of energy which state as [25],

$$\hbar\omega = E_g + \frac{(\hbar K)^2}{2\mu} \quad 2.13$$

Where E_g is the energy band gap and μ is the reduced electron- hole mass. Thus, for Photon energies less than $\hbar\omega$ and above $\hbar\omega$, the density of states term is zero. So $g(\hbar\omega)$, becomes

$$g(\hbar\omega) = \frac{1}{2\pi^2} \left(\frac{2\mu}{\hbar^2} \right)^{3/2} (\hbar\omega - E_g)^{1/2} \quad 2.14$$

Now getting back to I

$$I = -\frac{c}{8\pi} |\vec{E}^2| = \frac{c}{8\pi} \frac{\omega^2}{c^2} |\vec{A}|^2 = \frac{\omega^2}{8\pi c} |\vec{A}|^2 \quad 2.15$$

Rewriting α using equation (2.3) and simplifying the equation and putting the constants into a constant B we get:

$$\alpha = B \frac{(\hbar\omega - E_g)^{1/2}}{\hbar\omega} \quad 2.16$$

$$(\alpha\hbar\omega)^2 = B^2(\hbar\omega - E_g) \quad 2.17$$

2.2.2 Fresnel's equations

When an electromagnetic plane wave strikes the interface between two media of a dielectric with indices of refraction n_i and n_t , both reflected and refracted waves are generally produced. The angles of reflected and refracted waves are expressed by snell's law [26]:

$$n_i \sin \theta_i = n_t \sin \theta_t \quad 2.18$$

where n_i is indices of incident beam , n_t indices of transmitted beam, θ_i angle of incident beam and θ_t angle of transmitted beam.

From the Maxwell equations, a dispersion relation $k^2 = \varepsilon \left(\frac{\omega}{c}\right)^2$ is obtained relating the time variation with the spatial variation of the perturbation. In general, the wave vector k and the dielectric constant ε are complex quantities, that is, $\tilde{k} = k_1 - ik_2$ and $\tilde{\varepsilon} = \varepsilon_1 - i\varepsilon_2$. It is useful to define a complex index of refraction as [27]:

$$\tilde{n} = \tilde{k} \left(\frac{c}{\omega}\right) = n - ik \quad 2.19$$

For isotropic materials, k_1 and k_2 are parallel and,

$$\varepsilon_1 = n^2 - k^2 \quad 2.20(a)$$

$$\varepsilon_2 = 2nk \quad 2.20(b)$$

With the converse equations,

$$n^2 = \frac{1}{2} [\varepsilon_1 + (\varepsilon_1^2 + \varepsilon_2^2)^{1/2}] \quad 2.21(a)$$

$$k^2 = \frac{1}{2} [-\varepsilon_1 + (\varepsilon_1^2 + \varepsilon_2^2)^{1/2}] \quad 2.21(b)$$

Where k is the extinction coefficient

In order to construct relation between the measured reflectance and optical constants, we obtain the following derivation, since At normal incidence, $r = \frac{n_t - n_i}{n_t + n_i}$ through equation (2.18),so

$$R = r^2 = \left(\frac{\frac{n_t}{n_i} - 1}{\frac{n_t}{n_i} + 1} \right)^2 \quad 2.22$$

Since $n_i=1$ (air and film), then $n=n_t$ and for normal incidence conduction

Substituting equation 2.19 in R gives us

$$R = \frac{n^2 - 2n + 1 + k^2}{n^2 + 2n + 1 + k^2} = \frac{(n-1)^2 + k^2}{(n+1)^2 + k^2} \quad 2.23$$

Where,

$$k = \frac{\alpha\lambda}{4\pi} \quad 2.24$$

We see that in the low frequency limit $n \approx k$ and that n and k are both large we can rewrite equation (2.23) in the form

$$R = \frac{n^2 + k^2 - 2n}{n^2 + k^2 + 2n} \quad 2.25$$

Then,

$$R(n^2 + k^2 + 2n) = (n^2 + k^2 - 2n) \quad 2.26$$

$$(Rn^2 + Rk^2 + 2nR) = (n^2 + k^2 - 2n) \quad 2.27$$

$$n^2(R - 1) + k^2(R - 1) + 2n(R + 1) = 0 \quad 2.28$$

We divide equation 2.28 by (R-1) then it becomes,

$$n^2 + k^2 + 2n \frac{R+1}{R-1} = 0 \quad 2.29(a)$$

Let $\frac{R+1}{R-1} = D$ so

$$n^2 + 2nD + k^2 = 0 \quad 2.29(b)$$

This equation is solved to find a formula for n:

$$n = \frac{-2D \pm \sqrt{4D^2 - 4k^2}}{2} \quad 2.30(a)$$

$$n = \frac{-2\left(\frac{R+1}{R-1}\right) \pm \sqrt{4\left(\frac{R+1}{R-1}\right)^2 - 4k^2}}{2} \quad 2.30(b)$$

When we look to equation (2.30), we find the two roots involved, these roots are squared and separated in two solutions:

$$n = \frac{-2\left(\frac{R+1}{R-1}\right) + \sqrt{4\left(\frac{R+1}{R-1}\right)^2 - 4k^2}}{2} \quad 2.31(a)$$

$$n = \frac{-2\left(\frac{R+1}{R-1}\right) - \sqrt{4\left(\frac{R+1}{R-1}\right)^2 - 4k^2}}{2} \quad 2.31(b)$$

Since $n = \sqrt{\varepsilon_{eff}\mu_{eff}}$ where ε_{eff} and μ_{eff} are the effective permittivity and permeability, respectively and for nonmagnetic material ($\mu_{eff}=1$). Therefore, $n = \sqrt{\varepsilon_{eff}}$.

Where $\varepsilon_{eff} = \varepsilon_r - i\varepsilon_{im}$, ε_r and ε_{im} are the real and imaginary dielectric constant which can be written as [28]

$$\varepsilon_{im} = 2\sqrt{\varepsilon_{eff}} k \quad 2.32(a)$$

$$\varepsilon_r = \varepsilon_{eff} - k^2 \quad 2.32(b)$$

2.3 Drude- Lorentz Model

In the generalized Drude-Lorentz model, a number of simple poles having complex weights describe the permittivity in the complex frequency plane, which is a physically relevant and mathematically simple approach: By construction, it respects causality represents physical resonances of the material, and can be implemented easily in numerical simulations [24]. In Drude-Lorentz model, a group of atoms (N_a) per unit volume represent a dielectric material distributed in a vacuum. A field of electrons surround the atoms that themselves assumed to move in a vacuum around the atoms to which they are attached [30-]. The equation of motion that describes the electron motion is expressed as follows [31].

$$m_0 \frac{d^2x}{dt^2} + m_0 \gamma \frac{dx}{dt} + m_0 \omega_o^2 x = -eE \quad 2.33$$

Where m_0 is the electron mass, x is the electron displacement, γ is the damping coefficient, e is the electron charge, and E is the electric field. The former equation left side involves an

accelerating, damping, and force restored terms. On the other hand, the right side includes the driving force term.

We transact with an incident light electric field with a frequency the electric field is time dependent and introduce by the following equation [26]:

$$E(t) = E_0 \cos(\omega t + \phi) = E_0 \operatorname{Re}(\exp(-i\omega t - \phi)) \quad 2.34$$

Where E_0 and ϕ are the electric field amplitude and the light phase, respectively. The AC electric field brings on oscillation that have form,

$$X(t) = X_0 \operatorname{Re}(\exp(-i\omega t - \phi')) \quad 2.35$$

Where X_0 is the amplitude of the electron displacement, and ϕ' is the oscillation phase. We can substitute ϕ and ϕ' into electric field and displacement amplitudes. Moreover, E_0 and X_0 must be complex numbers. By inserting the equations of the electric field (2.34) and the expected displacement performance (2.35) in the equation of motion (2.33),

$$-m_0 \omega^2 X_0 e^{-i\omega t} - i m_0 \gamma \omega X_0 e^{-i\omega t} + m_0 \omega_o^2 X_0 e^{-i\omega t} = -e E_0 e^{-i\omega t}$$

The previous equation entails,

$$X_0 = - \frac{\frac{e E_0}{m_0}}{\omega_o^2 - \omega^2 - i \gamma \omega} \quad 2.36$$

A time dependent dipole moment $p(t)$ results from the frequency variant displacement amplitude denoted in equation (2.36), participates in the resonant polarization induction. Polarization is defined as the dipole moment per unit volume.

$$P_{\text{resonant}} = Np = -NeX \quad 2.37$$

$$\frac{Ne^2}{m_0} \frac{1}{\omega_0^2 - \omega^2 - i\gamma\omega} E$$

N is the number of atoms per unit volume. Equation (2.37) illustrates that polarization maximizes when the electric field frequency approaches ω_0 . This implies that the oscillation is ignored except if the incident light frequency is consistent with the material natural frequency ω_0 . Electric displacement D of a solid is polarization and electric field dependent [31].

$$D = \epsilon_0 E + P \quad 2.38$$

As we said before, oscillations are ignored unless $\omega = \omega_0$. Thus, polarization can be categorized into a resonant and non-resonant parts.

$$D = \epsilon_0 E + P_{\text{background}} + P_{\text{resonant}} \quad 2.39 (a)$$

$$D = \epsilon_0 E + \epsilon_0 \chi E + P_{\text{resonant}} \quad 2.39 (b)$$

Where χ is the electric susceptibility. In our seeking for the imaginary dielectric constant, the material is postulated to be isotropic. Isotropic expression proposes that the material possesses the same characteristics in all directions, and having no preferred axes. With this assumption, the electric displacement can be redefined as

$$D = \epsilon_0 \epsilon_r E \quad 2.40$$

Where ϵ_r is the relative dielectric constant. By employing the previous equation (2.40), the dielectric function described by the Drude-Lorentz model can be used to obtain the dispersion relation [20]:

$$\epsilon(\omega) = \sum_i^N \frac{w_{pei}^2}{(\omega^2 + i\omega\gamma_i)} + \sum_i^N \frac{w_{pei}^2}{(\omega_{ei}^2 - \omega^2) + i\omega\gamma_i} \quad 2.41$$

Where i refers to the relative peak. $w_{pe} = \sqrt{\frac{4\pi n e^2}{m^*}}$ is the electron bounded plasma frequency. n and m^* are the free electron density and the effective mass of free electrons, respectively. ω being the reduced resonant frequency, and γ is the damping rate. This model enables taking advantage of semiconductors at optical frequencies and searching for a possibility of an optical plasmon existence in that range.

This formula can be rearranged, in order to separate the real and imaginary dielectric constants. ϵ_1 and ϵ_2 are then obtained to be,

$$\epsilon_1(\omega) = 1 + \chi + \frac{N e^2}{\epsilon_0 m_0} \left(\frac{\omega_0 - \omega^2}{(\omega_0^2 - \omega^2)^2 + \gamma \omega^2} \right) \quad 2.42(a)$$

$$\epsilon_2(\omega) = \frac{N e^2}{\epsilon_0 m_0} \left(\frac{\omega \gamma}{(\omega_0^2 - \omega^2)^2 + \gamma \omega^2} \right) \quad 2.42(b)$$

By utilizing an incoming light of frequency ω , which is compatible with the material natural resonant frequency ω_0 , the assumption $\omega \approx \omega_0 \gg \gamma$ can be stated. $(\omega_0^2 - \omega^2)$ term can be roughly approximated to $2\omega_0\Delta\omega$ [32].

Static dielectric constant ϵ_{st} can be clarified as the relative dielectric constant ϵ_r at $\omega = 0$, which designate the low frequency material permittivity in the presence of static electric fields

$$\epsilon_l(0) = \epsilon_{st} = 1 + \chi + \frac{N e^2}{\epsilon_0 m_0 \omega_0^2} \quad 2.43$$

The high frequency permittivity can be indicated by the relative dielectric constant at $\omega = \infty$,

$$\epsilon_r(\infty) = \epsilon_\infty = 1 + \chi \quad 2.44$$

By subtracting the last two equations (2.43) and (2.44),

$$\epsilon_{st} - \epsilon_\infty = \frac{N e^2}{\epsilon_0 m_0 \omega_0^2} \quad 2.45$$

Where i refer to the relative peak. $w_{pe} = \sqrt{4\pi n e^2 / m^*}$ is the electron bounded plasma frequency, n and m^* are the free electron density and the effective mass of free electrons, respectively, ω_0 being the reduced resonant frequency, and γ is the damping rate. This model enables taking advantage of semiconductors at optical frequencies and searching for a possibility of an optical Plasmon existence in that range.

2.4 Interbands

In a semiconductor at low frequencies, the principal electronic conduction mechanism is associated with free carriers. A new conduction process can occur when the photon energy increases and becomes comparable to the energy gap. A photon can excite an electron from an occupied state in the valence band to an unoccupied state in the conduction band. In this process the photon is absorbed, an excited electronic state is formed and a hole is left behind [27]. Photon states can go through interband transitions, in a direct analogy to

electronic transitions in semiconductors. Such photonic transitions have recently been demonstrated experimentally in silicon micro-ring resonators. (We note that such a transition is different from the adiabatic wavelength conversion processing that the transition involves at least two photonic states [33].

Urbach's rule During this transition process, if these electrons encounter disorder, it causes density of their states $\rho(h\nu)$, where $h\nu$ is the photon energy, tailing into the energy gap. This tail of $\rho(h\nu)$ extending into the energy band gap is termed as Urbach tail. Consequently, absorption coefficient $\alpha(h\nu)$ also tails off in an exponential manner and the energy associated with this tail is referred to as Urbach energy and can be calculated by the following equation:

$$\alpha(h\nu) = \alpha_0 \exp\left(\frac{h\nu}{E_u}\right) \quad 2.46$$

Where α_0 is a constant, ' $h\nu$ ' is the photon energy and E_u is the Urbach energy [34].

Chapter Three Experimental Details

3.1 Substrate cleaning

The glass substrates were cleaned using alcohol in order to remove dusts and contaminants from the out surface. Then, the samples were shaken in ultrasonic media at 60 °C for 20 min. The substrates were dried and inserted into the evaporation system.

3.2 Preparation of Cu doped InSe thin films

The InSe was weighted and the copper wire of 13.5 cm lengths and 70 mg of mass was cut to small pieces. Then the pieces of Cu and 0.15 grams of InSe were mixed with the pestle until it forms an apparently a homogeneous mixture. The mixture was located into tungsten boat which is already prepared for evaporation of the doped films. The boat containing (fig.3.1) powder were fixed inside a vacuum thermal evaporator prior to film deposition.

The physical vapor deposition system was used to grow the doped films. The glass substrates were located on the metal plate 20 cm above the source (item 2). There is a movable physical shutter control (item 3) above the evaporation source and under the substrates. It is used to avoid the random evaporation and to ensure uniform conditions throughout the whole duration of the deposition process. The system was closed and allowed to evacuate the air till the vacuum pressure reaches 10^{-5} mbar. Then, the shutter was open, the substrates and the quartz crystal monitor are exposed to the vapor. When the shutter was closed, the grown films thicknesses were about 1.0 μm . The thicknesses of the films were measured during evaporation by a crystal oscillator thickness monitor (item 4) that rely on the damping of an oscillating quartz crystal microbalance (QCM) through inertial loading to measure frequency shifts. QCM is used as the sensor.



Fig. 3.1: The 600 VCM evaporation system

3.3Thin Film Analysis

The x-ray diffraction, scanning electron microcopy, energy dispersive x-ray spectroscopy and ultraviolet - visible light spectrophotometry techniques were used to characterize the films.

3.4 X-ray diffraction

The structure of the films can be explored using the diffraction principle of the electromagnetic waves. By using Bragg equation to described diffraction process, in which the Miller indices of the crystal planes, the lattice constant and crystal structure are determined [35]. When a continuous beam of X-ray is incident on the crystal, the beam reflected from the upper surface travels closer than the one reflected from the lower surface. When the path difference is an integral multiples of the incident wavelength, a constructive interference will occur satisfying Bragg's law [36]. The obtained XRD data was carried out using Rikago Miniflex 600 diffractometer that consists of the following parts, as shown in Fig. 3.2:

- 1- Source of X-ray, with a wavelength equal to 1.5405 °A.
- 2- Collimator, which is a device for restricting the wavelength range.
- 3- Holder for the films.
- 4- Radiation detector.
- 5- Signal processor.



Fig. 3.2: Rikagu Miniflex 600 diffractometer.

3.5 Scanning Electron Microscopy (SEM) measurements

The scanning electron microscopy (SEM) with COXEM 200 instrument in our lab, is exploited to characterize the surface morphology thin films. SEM technique involves a focused beam of electrons in order to scan the surface of the samples based on the principle that secondary electrons will be produced by inelastic collisions of energetic primary electrons, which are then ejected from a sample since they are attracted to a grid under low potential and then accelerated by a higher potential toward the detector. The field emission gun creates the primary electrons with energy range from few keV to 50 keV. The secondary electrons have energies lower than that of the primary electrons by a factor of thousand. Thus, the electrons are emitted from a region that is a few angstroms from the surface of the sample. The emitted electrons signals are used to plot an (x-y) positioning in a form of matrix. Samples to be imaged, the beam is focused by a magnetic lens and then

raster-scanned on a surface [37]. In particular, the SEM images with 30000 and 60000 enlargements were recorded for our samples.



Fig. 3.3: The scanning electron microscope device.

3.6 Energy-dispersive X-ray spectroscopy (EDX)

The atomic contents of the films were recorded by using an energy-dispersive x-ray analyzer attached to the SEM system. In this technique, the composition of the sample elements is determined depending on the X-ray generation in which a unique set of characteristic x-ray for each element is produced and sorted depending on its energy. The system consists of x-ray generator e.g: semiconductor, solid-state detector, electronics and software. When the X-ray photon impinged the semiconductor, the electrons are knocked out from the semiconductor and produce a small current. The energy of the original X-ray can be calculated by measuring the current. Then, revealing a spectrum of the number of X-

rays detected at each energy. From the spectrum, the weight of each element can be determined. In our work, regions of $6 \times 6 \text{ mm}^2$ were scanned and the ratios of In, Se, Ga and S atoms were determined.

3.7 Optical Measurements

A thermo- scientific Evolution 300 spectrophotometer that is equipped with VeeMax II spectrophotometer (Fig 3.4) was used to measure the optical transmittance and reflectance of the thin films. The measurements were carried out at normal incidence of (15°) in a wavelength range of (300-1100 nm) and scanning speed of 1200 nm/ min. The data were collected and manipulated with Vision-I software program attached to the system.

The optical band gap, interband transitions, absorbability, dielectric spectra and optical conductivity were determined from the transmittance T% and reflectance R% measurements.

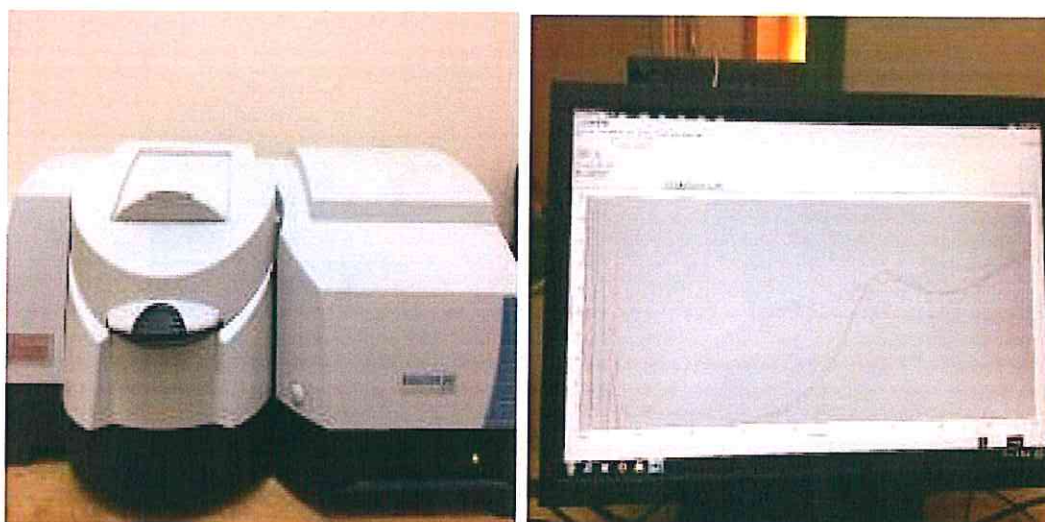


Fig. 3.4: The UV-VIS spectrophotometer.

Chapter Four

Results and Discussion

4.1 SEM and compositional analysis.

The scanning electron microscopy and energy dispersive X-ray spectroscopy analysis for the films under study were carried out using Coxem 200 equipped with EDAX unit. The scanning electron microscopy did not reveal any resolvable morphology or structure indicating the large degree of randomness and small crystallites. As appears in the inset of Fig. 4.1 (a), even for large magnifications no grains or crystallites were observed. On the other hand, the EDX spectra which is shown in Fig. 4.1 (a), (b) and (c) for the undoped and Cu-doped indium selenide thin films reveal the existence of glass ($\text{SiO}_2\text{:Na}_2\text{O:MgO:CaO}$) and indium, selenium and copper atoms only. No other foreign impurities were detected in the spectra. The appearance of Au peaks resulted from the surface coating to prevent electron contaminations. The results of the EDS analysis is shown in Table 4.1 While the undoped samples display approximately stoichiometric composition of indium selenide with some selenium deficiency, the doped samples displayed atomic content of 1.41% and 3.00%. The samples doped with 1.41 at. % Cu exhibit an empirical formula of the type $\text{In}_{30}\text{Se}_{70}$ ($\text{In}_{29}\text{Se}_{70}$). For the samples doped with 3.00% Excluding the Cu content one may find the empirical formula $\text{In}_{32}\text{Se}_{68}$. This form of Indium selenide which is achieved via Cu doping was previously obtained by heating a mixture of indium and selenium in an evacuated (5×10^{-5} Torr) glass capsule. The temperature of the system was elevated stepwise. In the first stage the capsule was heated at 513 K for 2 h. Then the temperature was raised to 653 K and heating was continued for 4 h. Finally, the temperature was raised

to 823 K and the capsule was heated for 14 h and quenched to room temperature. Bulky $\text{In}_{30}\text{Se}_{70}$ prepared by using this technique was observed to be of amorphous nature [38]. Optical band gap of thin film form of these samples which exhibit thickness of 250 nm is found to be 1.42 eV. The features of this material is rarely observed in literature and only a few articles can be found on $\text{In}_{30}\text{Se}_{70}$ films [39].

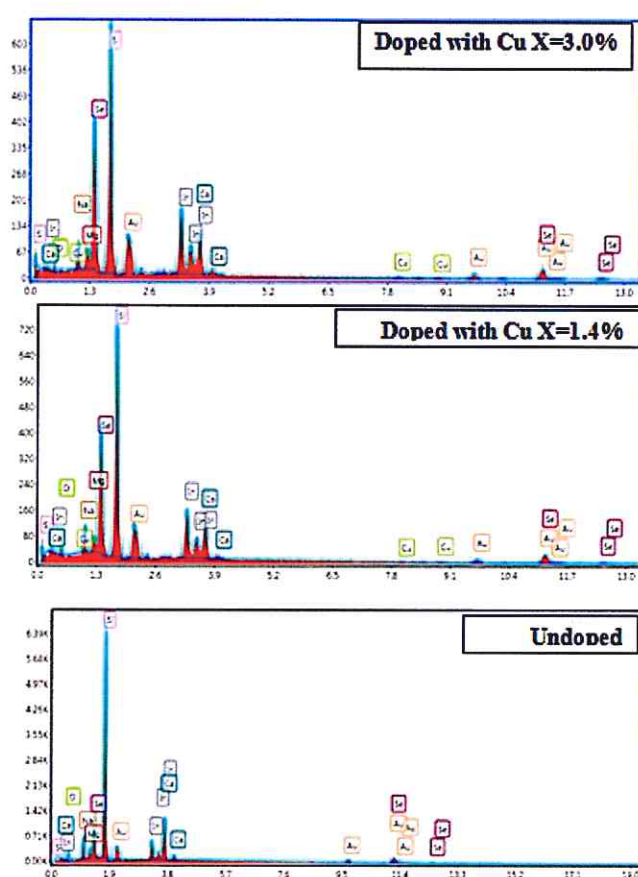


Fig. 4.1 The energy dispersive X-ray spectroscopy for (a) undoped and (b) 1.5 at. % doped and (c) 3.0 at. % copper doped indium selenide thin films.

sample	In at. %	Se at. %	Cu at. %	Se/In ratio
Undoped	51.6	48.4	0	0.94
Doped-1	28.93	69.66	1.41	2.41
Doped-2	31.00	66.00	3.00	2.13

4.2 Structural properties

Pure indium selenide and copper doped InSe thin films are subjected to X-ray diffraction analysis. The X-ray diffraction patterns which are illustrated in Fig 4.2 display no intensive peaks which indicate that the films are of amorphous nature. This result is consistent to literature data which indicate that InSe films grown onto glass substrate at room temperature by vacuum evaporation technique are amorphous in nature[40]. In addition, Fig4.2 also demonstrates the amorphous nature of the doped films. The appearance of the amorphous nature may be due to the statical occupation of the indium sites by In and Se which implies that there are In–In, In–Se and Se–Se near-neighbor correlations in the films. This leads to the presence of more than polymorphic phases of InSe which may lead to the random atomic distributions that on average display the amorphous nature [41]. It is also possible to assign the amorphous nature of InSe to the existence of more than polyphase of InSe at the same time. It is mentioned that InSe could exhibit α , β , γ and ϵ polymorphic phases depending on the melting temperature. For evaporation temperatures less than 500°C hexagonal α -In₂Se₃ is preferred [42]. Raising the temperature to 650 °C usually leads to the appearance of β -phase of In₂Se₃. When the temperature exceeds 650 °C γ -phase appears [43]. When the film comprises all these phases at a time, highly disordered material

is expected. The inability of Cu to play role in the structure maybe due to it is low doping level.

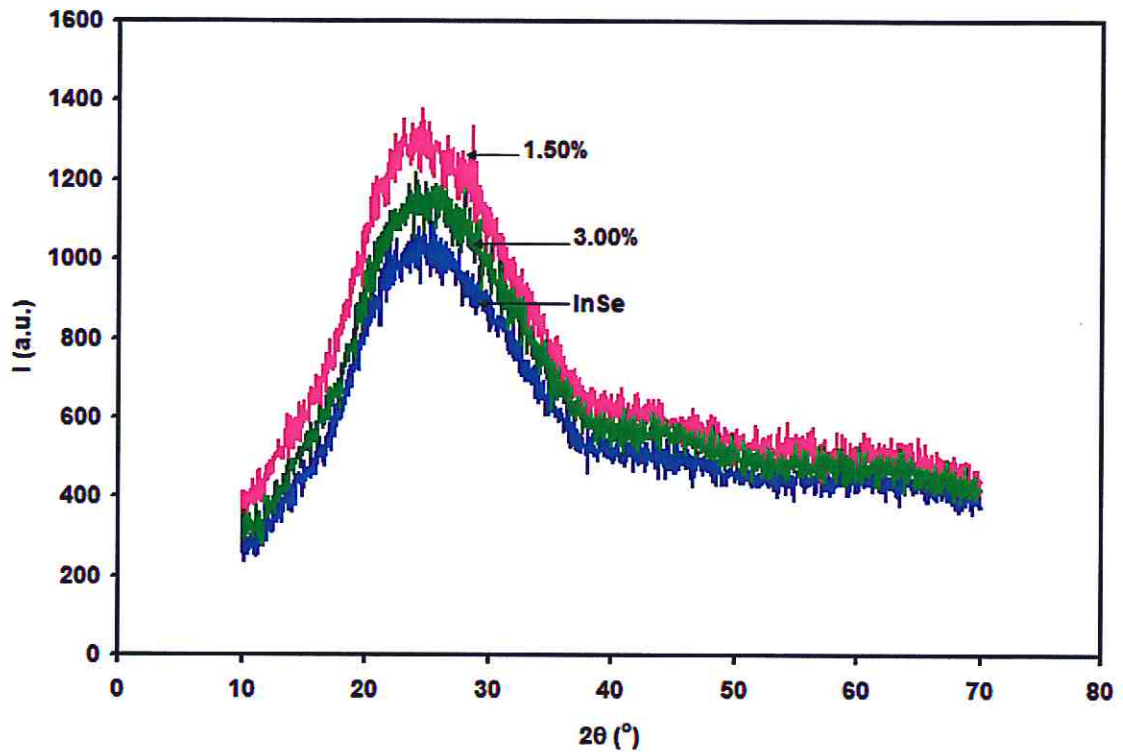


Fig. 4.2 XRD pattern of InSe, InSe doped with 1.50 at% Cu and InSe doped with 3.00 at% Cu thin films at room temperature.

4.3 Optical analysis

The spectral data of transmittance (T), reflectance (R) and the absorption coefficient (α) for the Cu doped InSe are studied using ultra-violet visible light spectrophotometry technique. The thickness of Cu doped InSe film is 1.0 μm . As it is readable from Fig. 4.3, the InSe thin films which are grown onto glass substrates are highly transparent in the spectral range of 500-850 nm. The transmittance spectra of InSe doped with 1.50 at% Cu films slightly

increases until it reaches value of 37% 634 nm, after that it nearly remains constant between (635-73 nm). In that range it increases rapidly. The transmittance spectra of InSe doped with 3.00 at% Cu films slightly increases in the range of 500-680 nm. It then decreases and reincreases, following the same trend of variation like that of samples doped with 1.50 at% Cu.

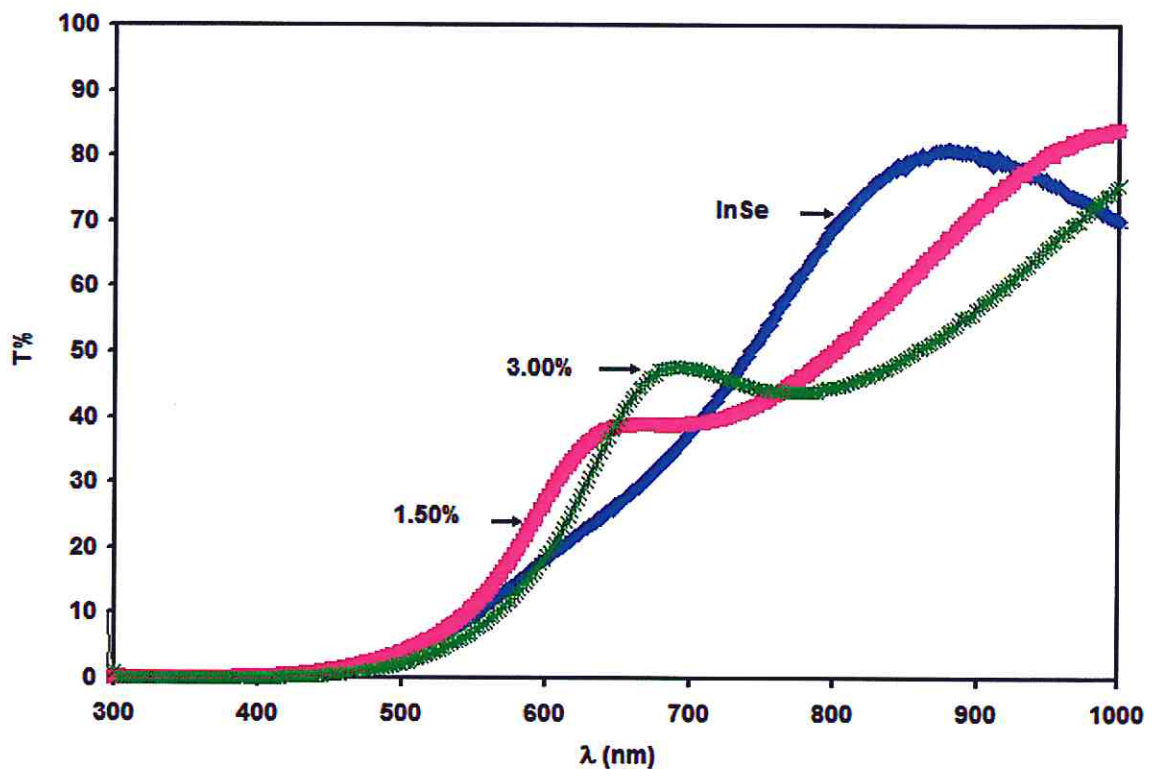


Figure 4.3: The transmittance spectra for InSe, InSe doped with 1.50 at% Cu and InSe doped with 3.00 at% Cu.

On the other hand, the reflectance spectra (R) for Cu doped InSe samples, which are shown in Fig 4.4, follows four stages of variations. Firstly, it shows wavelength independent reflectivity of 18% in the region (300-600 nm), then it increases reaching 30% at 700 nm. In the third region, it continues decreasing until λ reaches 900nm. In the region of 900-1100 nm it reincreases. In spite of having the same thickness, both of the InSe doped with 1.50

at% and 3.00 at% exhibit different reflectance spectra which display peaks at different positions. The doped InSe with 1.50 at% Cu exhibits one peak, at 722 nm. The doped InSe with 3.00 at% Cu exhibit two peaks, namely, at 568 nm and 808 nm.

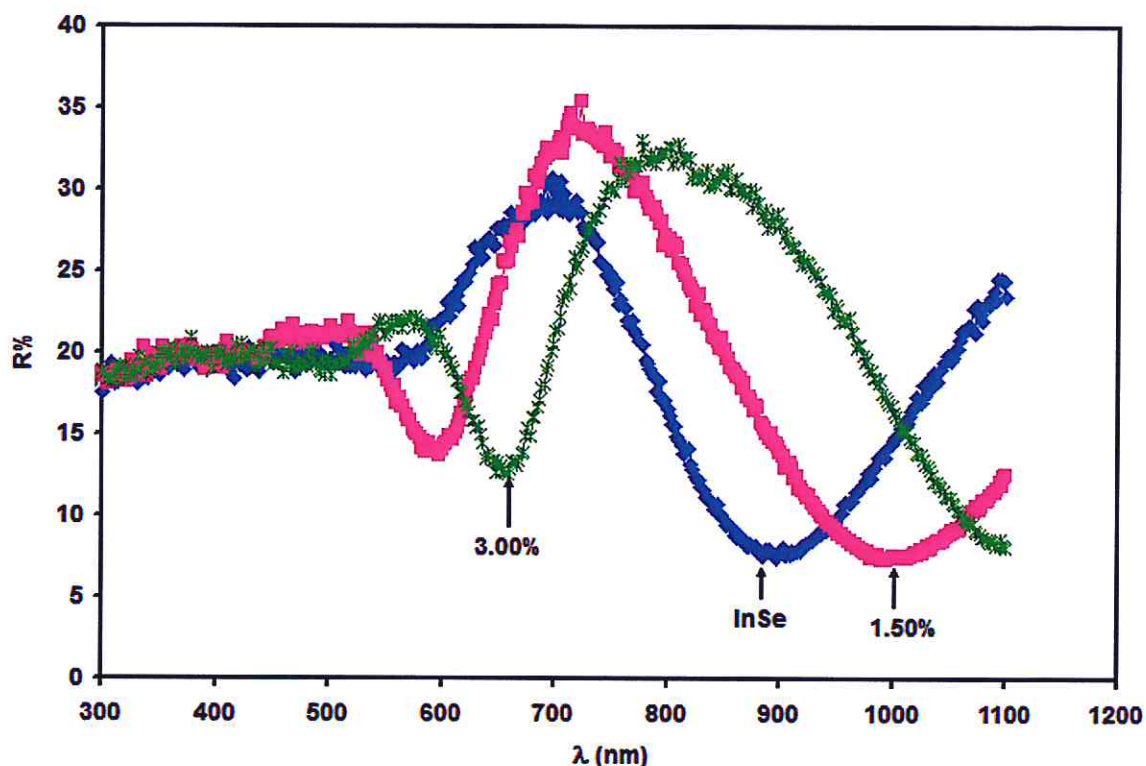


Figure 4.4: The reflectance spectra for InSe, InSe doped with 1.50 at% Cu and InSe doped with 3.00 at% Cu.

In order to get additional knowledge about the optical properties of the Cu doped InSe, the absorption coefficient spectra of the films were calculated with equation (2.2). The equation is described in the theoretical part for absorption due to multilayer plotted as function of incident photon energy. The relationship between the absorption coefficient (α) and the incident photon energy (E) is illustrated in the Fig 4.5.

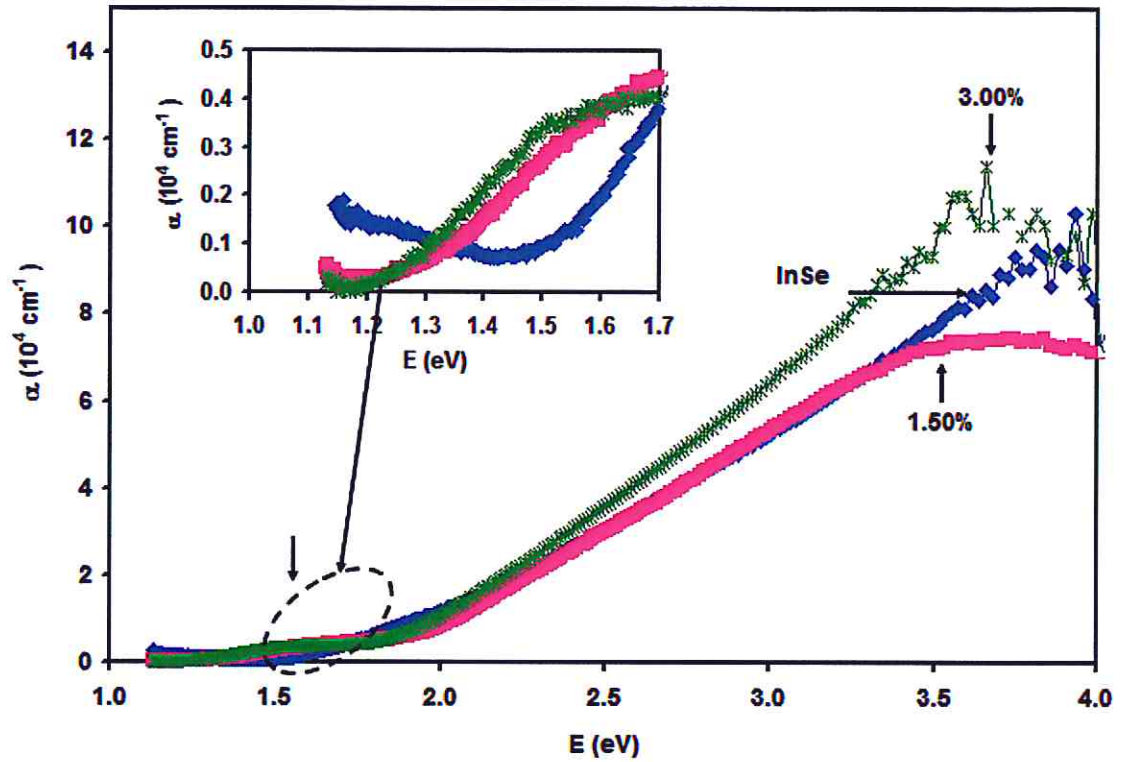


Figure 4.5: The relation between absorption coefficient (α) and the incident photon energy in (eV) for InSe, 1.50 % Cu doped InSe and 3.00% Cu doped InSe.

As it is also readable from the figure, the absorption coefficient (α) for InSe increases with increasing incident photon energy. It is shown in the inset of the figure, that the decay in α values for the doped samples is faster than that of undoped ones. Such behavior indicates strong attenuation in the band tail which leads to the formation of interbands. Interbands usually forms from inhomogeneities and high defect concentrations in addition to the incomplete bonding at the surface [44]. The absence of the interband in the presence of Cu should be assigned to the vacancy filling and the completeness of the bonds [45].

The ionic radius of In^{+3} is 0.94 \AA that of Cu^{+3} is 0.53 \AA [46,47]. It means that Cu^{+3} ion can

replace vacant sites of In^{+3} forming CuSe bonds. These bonds are expected to occupy places of unbonded regions. In this case, defect density decreases. Calculations of the interband transition widths (E_e) in accordance with Urbach's rule that are illustrated in Fig 4.6, reveal interbands of widths of 0.59, 0.13, 0.14 eV for the undoped samples and sample doped with Cu of content of 1.50 at% and 3.00%, respectively. The decrease in the interband width is also ascribed to that completed bonding owing to the vacancy filling by Cu in sites of In. The electronic configuration of In, Se, and Cu are, $4d^{10} 5s^2 5p^1, 3d^{10} 4s^2 4p^4$, and $4s^2 3d^9$, respectively [48,49,50], the Cu atoms with the unfilled $4d$ orbitals can easily overlap with $4p$ orbitals of selenide atoms leading to the formation of these band tails. The data of E_e suggests that Cu atoms reduce the width of the band tail through vacancy filling and orbital overlapping.

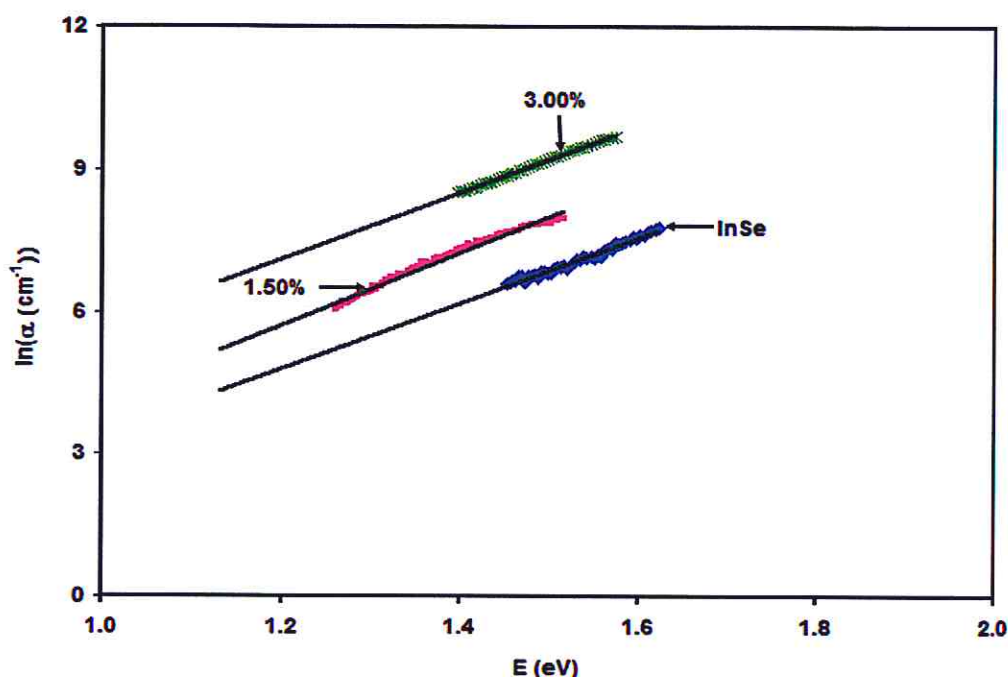


Figure 4.6: The $\ln(\alpha)$ -E variation for InSe, doped InSe with 1.50 at% Cu and doped InSe with 3.00 at% Cu.

To determine the energy band gap from the absorption coefficient spectra, $(\alpha E)^p$ versus photon energy, E , in accordance with Tauc's equation [51], $(\alpha E)^p = (E - E_g)$ were plotted. The value of p determines the type of the band gap. It has four values which can be 2 for direct allowed, $1/2$ for indirect allowed, $1/3$ for indirect forbidden and $2/3$ for direct forbidden electronic transitions. To know the types of band gaps for the films under study, the $(\alpha E)^2$, $(\alpha E)^{1/2}$, $(\alpha E)^{1/3}$, $(\alpha E)^{2/3}$ were plotted versus the photon energy. The plots which linearize the widest range of data were considered. As the result of comparing $(\alpha E)^2$ -E and $(\alpha E)^{1/2}$ -E plots we observed that for undoped samples and those doped with 1.50 at% Cu, the most appropriate fitting refers to the indirect allowed transition energy band gap with values of 1.38 and 1.50 eV, respectively. For the sample doped with 3.00 at% Cu, the

most appropriate fitting (Fig 4.6) refer to direct allowed transition energy band gaps of value of 1.65 eV.

Literature data reported value of 1.4 eV for indirect gaps of pure InSe [52], and value of 1.5-1.6 eV direct band gap. [53] On the other hand, for H- doped InSe the direct band gap value is reported to be 0.9 eV [54], for Cd doped InSe direct band gap value of 1.47 eV is reported. [55] The electronic band structure of InSe is consisted of indium s -like conduction bands(E_C) minimum and p -like valence bands(E_V) maximum with the direct band gap located at Z point of the Brillouin zone [56,57]. The representative band scheme of the InSe near band edges is depicted in the inset of Fig 4.7 for comparison. The top of E_V of InSe is constructed by Se p_z -like orbital [57] (i.e., as the inset shown in Fig 4.7) whereas the valence-band splitting may come from the Se p_x - and p_y -like states of InSe [58].

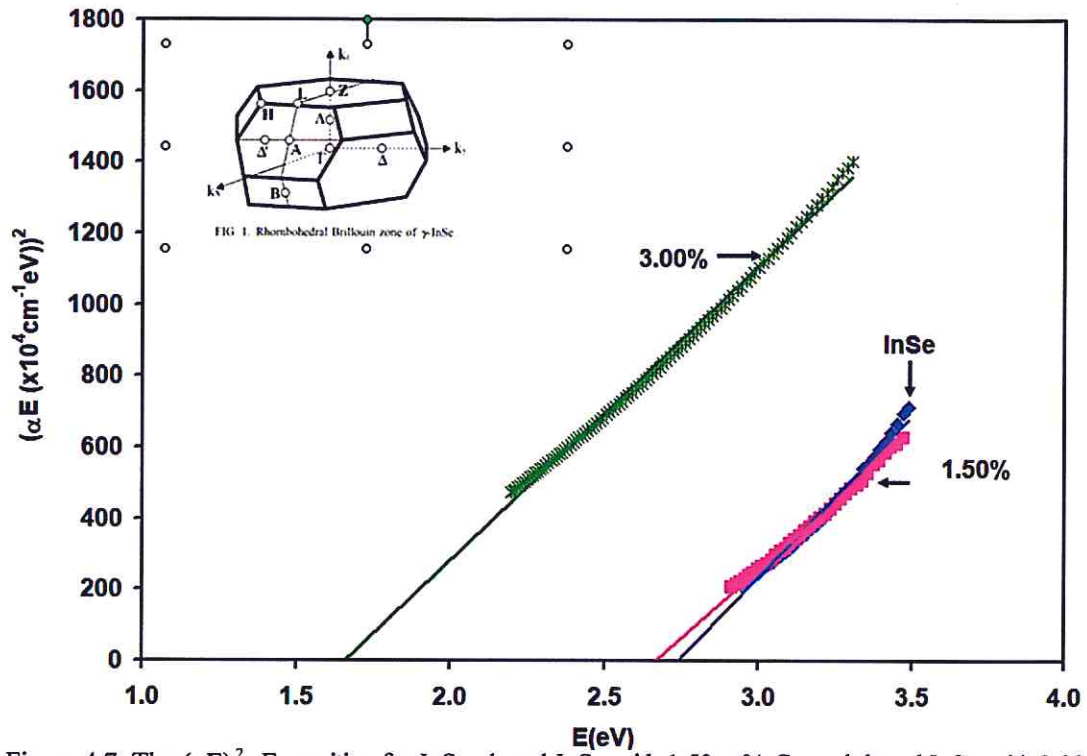


Figure 4.7: The $(\alpha E)^2$ - E variation for InSe, doped InSe with 1.50 at% Cu and doped InSe with 3.00 at% Cu.

In accordance to the Brillouin zone of InSe which belong to rhombohedral space group $C3V$ $5SR3md$. InSe exhibit direct band gap at the z point and becomes indirect if exposed to pressure [59]. Demonstrations of the band structure of InSe is presented in the inset of Fig 4.8.

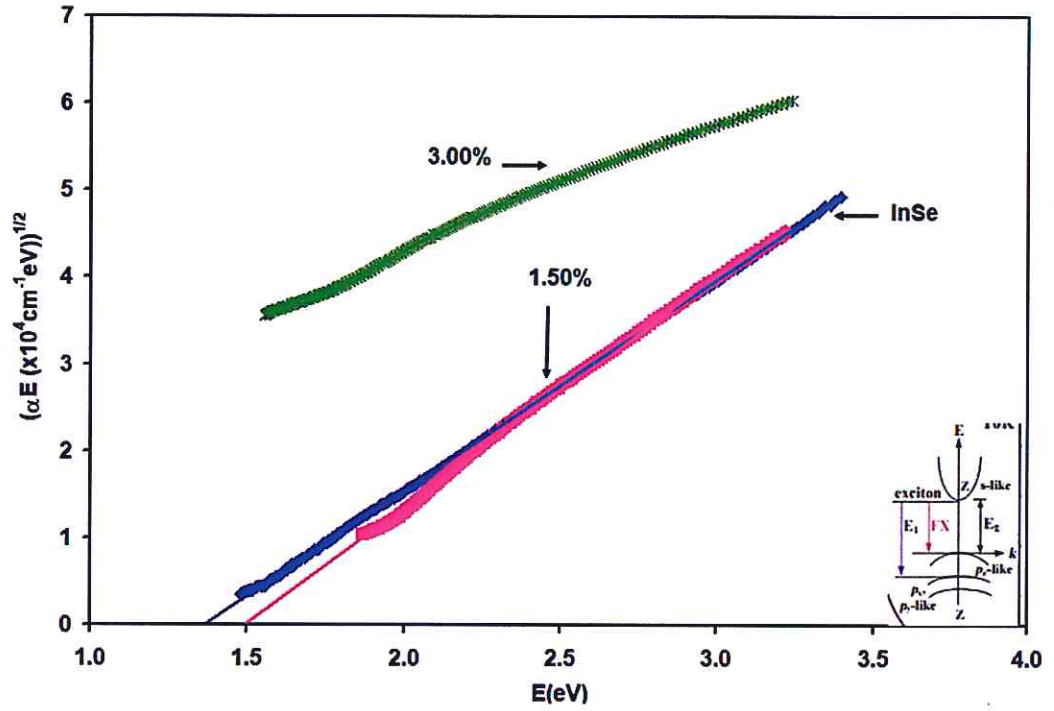


Figure 4.8: The $(\alpha E)^{1/2}$ -E variation for InSe, doped InSe with 1.50 at% Cu and doped InSe with 3.00 at% Cu.

The dielectric constant consists of two parts: real and imaginary. The real part of the dielectric constant is calculated using $\epsilon_r = \epsilon_{eff} - k^2$ where k is the extinction coefficient. $k = \frac{\alpha\lambda}{4\pi}$ and ϵ_{eff} being the effective dielectric constant spectra $\epsilon_{eff} = \epsilon_r + i\epsilon_{im}$ [60,61] which are determined from the reflectance and transmittance data with the help of Fresnel equations (2.22) that arrive at the result, where ($n^2 = \epsilon_{eff}$). ϵ_r spectra are presented in Fig 4.9. As shown from the figure, InSe shows one peak at 1.78 eV. However, doped InSe with 1.50 at% Cu and doped InSe with 3.00 at% Cu has peaks of values of 1.74 eV and 1.54 eV, respectively. By comparing these values with those obtained for the band gaps. The values of the band gap are not close to what resulted from the dielectric spectra.

The band gaps for InSe, doped InSe with 1.50 at% Cu and doped InSe with 3.00 at% Cu are 1.38, 1.50 and 1.68 respectively. It means that the dielectric dispersion can't be accounted for direct or indirect transitions from the valence to the conduction band. It is also observable that the doping of copper into InSe increase the value of the dielectric constant. Particularly, while the dielectric constant show maxima of value of 12, 15 and 13.5 for samples doped with 1.5% and 3.0% copper. The resonance peak which appears at 1.78 eV was previously observed in InSe and assigned to the direct allowed transitions from the valence to the conduction band of InSe at energy of 1.81 eV [62]. The peak which appeared at 1.54 eV may be ascribed to the transitions in β -CuS which displayed energy band gap of 1.54 eV when deposited at substrate temperature of 150 °C [63].

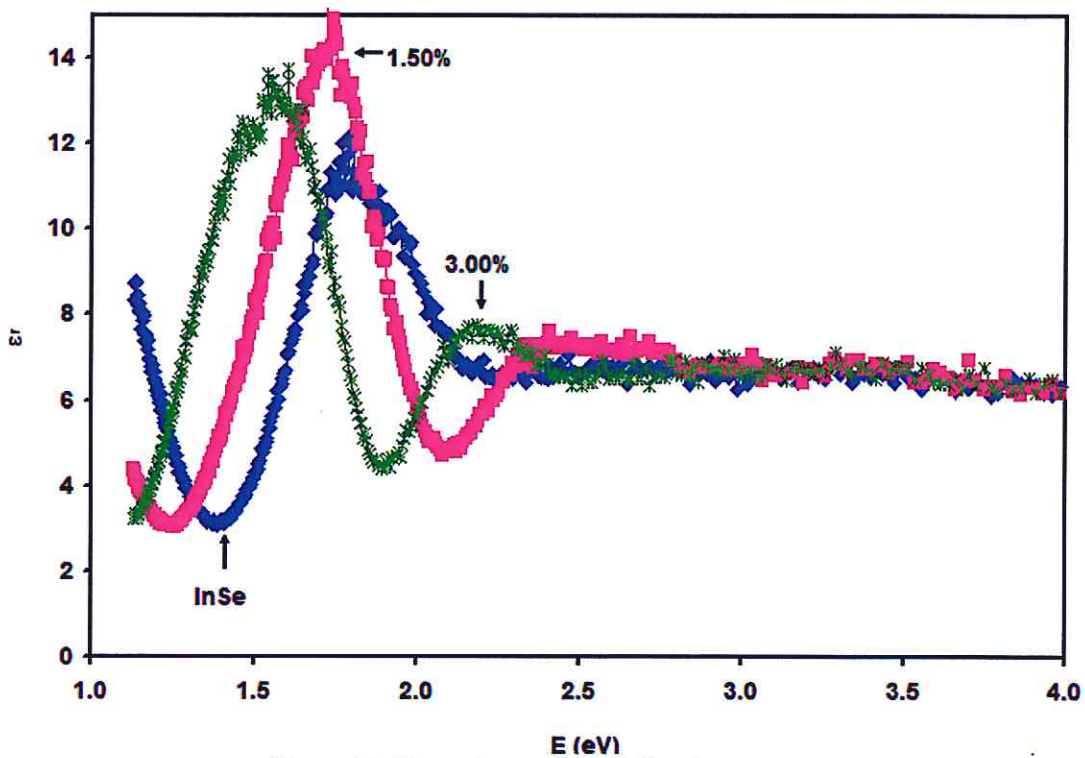


Figure 4.9: The real part of the dielectric constant.

The imaginary part of the dielectric spectra is shown in Fig 4.10. It is clear from the figure that ϵ_{im} always increase with increasing photon energy reaching a maximum near 3.0 eV. It is also evident from the figure that the higher, the doping the larger the ϵ_{im} value. This behavior mostly arises from the presence of more free electrons that are associated with the increase doping content.

To reveal information about optical signal quality, modeling of generalized Drude-Lorentz equation for the imaginary part of the dielectric constant was made. The using of Drude – Lorentz model assuming set of five linear oscillators was sufficient to produce the experimental data, the influence of damping forces whose coefficients (γ) are inversely proportional to the collision times (τ) of free charge as shown in the equation (2.22). is obtained. By using the effective masses for InSe and Cu, the experimental data were reproduced. The effective mass of InSe and Cu are $0.143m_0$ [64] and $1.2m_0$ [65], respectively. The effective mass of Cu doped InSe is determined by using $(m^*)^{-1} = (m_{InSe}^*)^{-1} + (m_{Cu}^*)^{-1}$. The estimated values are presented by, the collision time (τ_i), free charge carriers (n_i), angular frequency (ω_i) and the drift mobility ($\mu = e\tau/m$) are tabulated in table 4.2.

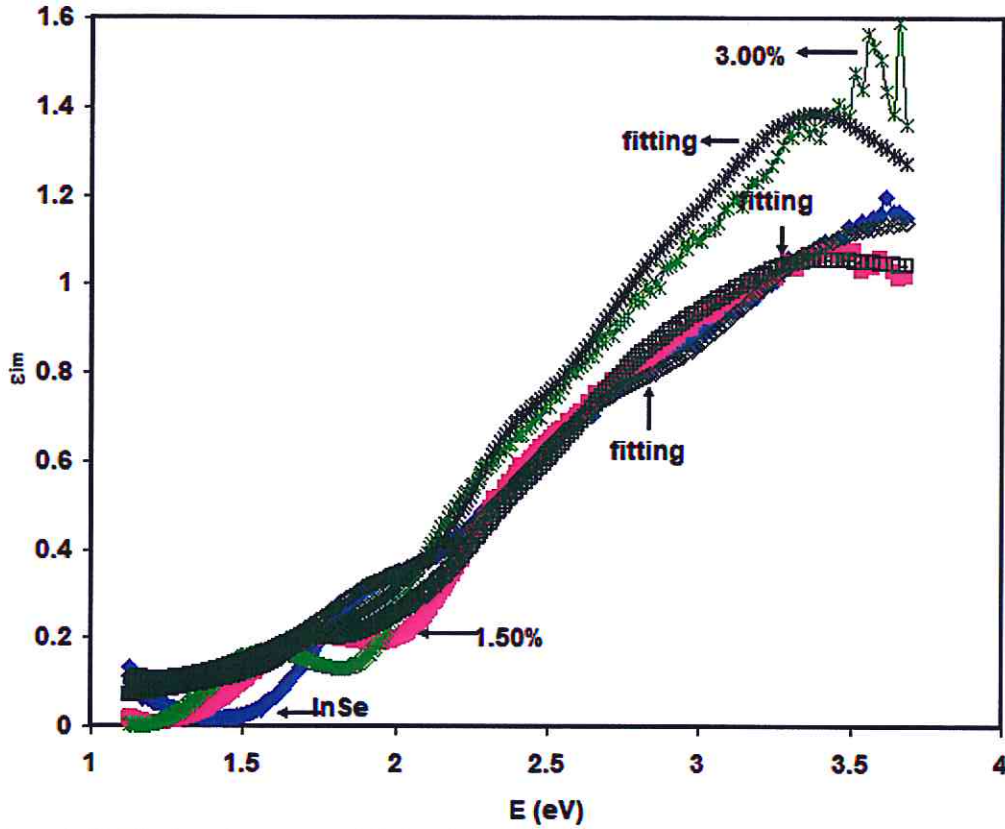


Figure 4.10: The imaginary part of dielectric constants for InSe, doped InSe with 1.50 at% Cu and doped InSe with 3.00 at% Cu. The black colored lines are fitting of the Drude –Lorentz equation.

As may be read from the table, with increasing number of oscillators ($k=1,2, \dots, 5$), the scattering time decrease indicating an increase in the damping coefficient values. This increase is accompanied with increase in the free carrier density, decrease in drift mobility and increase in the Plasmon frequency. This behavior is ascribed to the inability of the oscillators or dipoles to align with the incident light signal, thus it leaves the charge carriers free. On the other hand, for $k=1$ remarkable increase in the values of reduced frequency from 1.7×10^{15} Hz to 0.6×10^{15} Hz, in the free carrier density from 5×10^{16} to $1 \times 10^{17} \text{ cm}^{-3}$, in the drift mobility value from $43 \text{ cm}^2/\text{Vs}$ to $55 \text{ cm}^2/\text{Vs}$ and in the Plasmon frequency from 0.35 to 0.52 GHz is obtained upon doping InSe with 1.5% Cu increasing the Cu content further,

decreases the fitting parameters slightly indicating that the optimum doping should be near 1.5% only .the fitting parameter which are obtained here are much high than those reported for InSe films coated on to Au and yttrium thin film substrates[66].

Table 4.1: The fitting parameters of Drude-Lorentz model for InSe, doped InSe with 1.50 at% Cu and doped InSe with 3.00 at% Cu.

	InSe					doped InSe with 1.50 at% Cu					doped InSe with 3.00 at% Cu				
	1	2	3	4	5	1	2	3	4	5	1	2	3	4	5
$\tau_i(\text{fs})$	3.5	1.5	0.60	0.65	0.60	4.00	1.60	0.65	0.65	0.59	3.0	1.7	0.68	0.65	0.50
$w_e (\times 10^{15})$	1.70	2.90	4.10	5.10	5.90	2.60	3.60	4.30	5.05	5.90	2.0	3.6	4.3	5.1	6.0
$n(\times 10^{17} \text{ cm}^{-3})$	0.50	5.0	100	135	280	1.0	5.0	90	120	220	0.1	10	90	190	280
$\mu (\text{cm}^2/\text{Vs})$	43.0	18.4	7.37	7.99	7.37	55.0	22.0	8.94	8.94	8.11	41.3	23.4	9.35	8.94	6.88
$w_{pi}(\text{GHz})$	0.351	1.11	4.97	5.77	8.31	0.52	1.2	4.9	5.8	7.8	0.16	1.6	4.9	7.2	8.8

Chapter Five

Conclusion

In this work we have studied the copper doping effects on the structural, optical and dielectric properties of indium selenide thin films. A copper doping content of 3.0at % was sufficient to change the nature of the band transitions from indirect to direct allowed electronic transitions without altering the amorphous nature of the films. The formed films preferred the chemical interactions that for m_s $\text{In}_{30}\text{Se}_{70}$ in the presence of Cu. Cu doping also succeed in reducing the width of the band tails which already exists in the band gap of InSe. In addition a blue shift in the energy band gap value from 1.38 to 1.50 eV is achieved upon doping InSe with Cu of atomic content of 1.5 at%. The band gap reached value of 1.74 when Cu content is increased to 3.0 at%. Moreover, doping of InSe with copper is observed to enhance the dielectric property significantly, the dielectric spectra shifts toward lower energy values as a results of Cu-Se interactions. Furthermore, the modeling's of the imaginary part of the dielectric spectra with the Drude-lorentz approach for optical conduction have shown that all the conduction parameters presented by scattering time at femto second level, drift mobility, free carrier density and Plasmon frequency are all increased upon insertion of 1.5 at% Cu into the structure of InSe making it more appropriate for optoelectronic applications.

References

- [1] A Qasrawi, A. F. (2018). Investigation of the structural and optoelectronic properties of the Se/Ga₂S₃ heterojunctions. *Journal of Alloys and Compounds*, 769, 78-82.
- [2] Diaz, L. (2019). *Impact of Leader-Member Exchange and Leadership Styles of Nurse Middle Managers on the Knowledge Sharing Behaviors of Registered Nurses*. Central Michigan University.
- [3] Yang, Y., Jeon, J., Park, J. H., Jeong, M. S., Lee, B. H., Hwang, E., & Lee, S. (2019). Plasmonic Transition Metal Carbide Electrodes for High-Performance InSe Photodetectors. *ACS nano*, 13(8), 8804-8810.
- [4] Song, C., Fan, F., Xuan, N., Huang, S., Zhang, G., Wang, C., ... & Yan, H. (2018). Largely tunable band structures of few-layer InSe by uniaxial strain. *ACS applied materials & interfaces*, 10(4), 3994-4000..
- [5] Das, M. R., & Mitra, P. (2018). Influence of nickel incorporation on structural, optical and electrical characteristics of SILAR synthesized CuO thin films. *Journal of Sol-Gel Science and Technology*, 87(1), 59-73.
- [6] Jain, V. K., & Kedarnath, G. (2018). Applications of metal selenium/tellurium compounds in materials science. *Physical Sciences Reviews*, 4(5).
- [7] Patel, P., Patel, V., Vyas, S., Patel, J., & Pavagadhi, H. (2019). Optical Investigations of In₂Se₂. 7Sb_{0.3} Thin Films Prepared by Thermal Evaporation Technique. In *Materials Science Forum* (Vol. 969, pp. 355-360). Trans Tech Publications Ltd.
- [8] Wells, S. A., Henning, A., Gish, J. T., Sangwan, V. K., Lauhon, L. J., & Hersam, M. C. (2018). Suppressing Ambient Degradation of Exfoliated InSe Nanosheet Devices via Seeded Atomic Layer Deposition Encapsulation. *Nano letters*, 18(12), 7876-7882.
- [9] Megido, R. C., Poelaert, C., Ernens, M., Liotta, M., Blecker, C., Danthine, S., ... & Francis, F. (2018). Effect of household cooking techniques on the microbiological load and the nutritional quality of mealworms (*Tenebrio molitor* L. 1758). *Food research international*, 106, 503-508.
- [10] Jalali Sarvestani, M. R. (2018). Investigating the Effect of Doping Graphene with Silicon in the Adsorption of Alanine by Density Functional Theory. *Physical Chemistry Research*, 6(3), 639-655.
- [11] Wan, S., Li, Y., Li, W., Mao, X., Wang, C., Chen, C., ... & Zhu, W. (2019). Nonvolatile Ferroelectric Memory Effect in Ultrathin α -In₂Se₃. *Advanced Functional Materials*, 29(20), 1808606.
- [12] Ertap, H., & Karabulut, M. (2018). Structural and electrical properties of boron doped InSe single crystals. *Materials Research Express*, 6(3), 035901.

- [13] Growth and Characterizations of Cd-Doped InSe Films BY N. BENRAMDANE, J. P. GUESDON, and C. JULIEN~)
- [14] Zhao, B., Wolter, S., & Greenberg, J. A. (2018, May). Application of machine learning to x-ray diffraction-based classification. In *Anomaly Detection and Imaging with X-Rays (ADIX) III* (Vol. 10632, p. 1063205). International Society for Optics and Photonics.
- [15] Xue, C., Meng, X., Wu, Y., Wang, Y., Wang, L., Yang, S., ... & Tai, R. (2018). The wave optical whole process design of the soft X-ray interference lithography beamline at SSRF. *Journal of synchrotron radiation*, 25(6), 1869-1876.
- [16] Bykkam, S., Ahmadipour, M., Narisngam, S., Kalagadda, V. R., & Chidurala, S. C. (2015). Extensive studies on X-ray diffraction of green synthesized silver nanoparticles. *Adv. Nanopart*, 4(1), 1-10.
- [17] Nguyen, T. D., Sierra, E., Eguiraun, H., & Lizundia, E. (2018). Iridescent cellulose nanocrystal films: the link between structural colour and Bragg's law. *European Journal of Physics*, 39(4), 045803.
- [18] Kumar, Challa SSR, ed. X-ray and Neutron Techniques for Nanomaterials Characterization. Springer Berlin Heidelberg, 2015.
- [19] Charles Kittel-Introduction to Solid State Physics-Wiley (2005)/8th edition
- [20] Milosevic, Milan. Internal reflection and ATR spectroscopy. Vol. 262. John Wiley & Sons, 2012.
- [21] Salman, Y. A., Abdullah, O. G., Hanna, R. R., & Aziz, S. B. (2018). Conductivity and electrical properties of chitosan-methylcellulose blend biopolymer electrolyte incorporated with lithium tetrafluoroborate. *Int. J. Electrochem. Sci*, 13, 3185-3199.
- [22] Hinrichs, K., & Eichhorn, K. J. (Eds.). (2018). *Ellipsometry of functional organic surfaces and films* (Vol. 52). Springer.
- [23] Bauer, E. (2014). *Surface microscopy with low energy electrons* (Vol. 23). New York: Springer.
- [24] Quinten, M. (2010). *Optical properties of nanoparticle systems: Mie and beyond*. John Wiley & Sons.
- [25] Jermyn, A. S., Tagliabue, G., Atwater, H. A., Goddard III, W. A., Narang, P., & Sundararaman, R. (2019). Transport of hot carriers in plasmonic nanostructures. *Physical Review Materials*, 3(7), 075201.

- [26] Abdullah, O. G., Aziz, S. B., & Saber, D. R. (2018). Characterizations of pure and Pb²⁺ ion doped methylcellulose based biopolymer electrolyte films: Optical and electrical properties. *Int. J. Electrochem. Sci*, 13, 11931-11952.
- [27] Dresselhaus, M. S. (2001). Solid state physics part ii optical properties of solids
- [28] Born, M., & Wolf, E. (2013). *Principles of optics: electromagnetic theory of propagation, interference and diffraction of light*. Elsevier.,
- [29] Eldlio, Mohamed, Franklin Che, and Michael Cada. "Drude-Lorentz Model of Semiconductor Optical Plasmons." IAENG Transactions on Engineering Technologies. Springer Netherlands, 2014. 41-49.
- [30] Sehmi, H. S., Langbein, W., & Muljarov, E. A. (2017). Optimizing the Drude-Lorentz model for material permittivity: Method, program, and examples for gold, silver, and copper. *Physical Review B*, 95(11), 115444.
- [31] Basic Electromagnetism and Materials P231, André Moliton - 2006
- [32] Dorfman, K. E., Asban, S., Ye, L., Rouxel, J. R., Cho, D., & Mukamel, S. (2019). Monitoring spontaneous charge-density fluctuations by single-molecule diffraction of quantum light. *The journal of physical chemistry letters*, 10(4), 768-773..
- [33] " *Nature photonics* 3, no. 2 (2009): 91.
- [34] Sharma, N., Sharma, S., Prabakar, K., Amirthapandian, S., Ilango, S., Dash, S., & Tyagi, A. K. (2015). Optical band gap and associated band-tails in nanocrystalline AlN thin films grown by reactive IBSD at different substrate temperatures. *arXiv preprint arXiv:1507.04867*.
- [35] Klein, Andreas. Origins of limited electrical performance of polycrystalline Cu₂O thinfilm transistors. Diss. Faculdade de Ciências e Tecnologia, Universidade NOVA de Lisboa, 2017
- [36] Askeland, Donald R., and Wendelin J. Wright. Science and Engineering of Materials. Nelson Education, 2015.
- [37] Reimer, Ludwig. "Scanning electron microscopy: physics of image formation and microanalysis." (2000): 1826.
- [38] Chaudhuri, S., S. K. Biswas, and A. Choudhury. "Effects of heat treatment on the optical absorption of amorphous In₃₀Se₇₀ films." *Physica Status Solidi. A, Applied Research* 83, no. 1 (1984): K57-K60.
- [39] Chaudhuri, S., S. K. Biswas, and A. Choudhury. "The optical energy gap of amorphous In₃₀Se₇₀ films." *Physica Status Solidi. A, Applied Research* 93, no. 1 (1986): K47-K49.

- [40] SOLID STATE PHYSICS PART II Optical Properties of Solids M. S. Dresselhaus, 15
- [41] QASRAWI, A. F.; SHEHADA, Sufyan R. Dielectric dispersion in InSe/CdS bilayers. *Physica E: Low-dimensional Systems and Nanostructures*, 2018, 103: 151-155.
- [42] Qasrawi, A. F., & Shehada, S. R. (2018). Dielectric dispersion in InSe/CdS bilayers. *Physica E: Low-dimensional Systems and Nanostructures*, 103, 151-155.
- [43] Jain, V. K., & Kedarnath, G. (2018). Applications of metal selenium/tellurium compounds in materials science. *Physical Sciences Reviews*, 4(5).
- [44] Pankove, Jacques I. Optical processes in semiconductors. Courier Corporation, 2012.
- [45] Rani, S., Rajan, S. T., Shanthi, J., Ayeshamariam, A., & Jayachandran, M. (2015). Review on the Materials Properties and Photoelectrochemical (PEC) Solar Cells of CdSe, Cd_{1-x}Zn_xSe, Cd_{1-x}In_xSe, Thin Films. In *Materials Science Forum* (Vol. 832, pp. 1-27). Trans Tech Publications..
- [46] Tranquada, J. M., Heald, S. M., & Moodenbaugh, A. R. (1987). X-ray-absorption near-edge-structure study of La_{2-x}(Ba_xSr_{1-x})CuO_{4-y} superconductors. *Physical Review B*, 36(10), 5263.
- [47] Gautam, Subodh K., Fouran Singh, S. Ojha, R. G. Singh, and VV Siva Kumar. "Decomposition mechanism of indium oxide nanoparticles sandwiched between zinc oxide layers by energetic ions." *Ceramics International* 42, no. 2 (2016): 2846-2853.
- [48] Zhao, W., Ghorannevis, Z., Chu, L., Toh, M., Kloc, C., Tan, P. H., & Eda, G. (2012). Evolution of electronic structure in atomically thin sheets of WS₂ and WSe₂. *ACS nano*, 7(1), 791-797.
- [49] S.K. Jain & Shailesh K. Jain, Conceptual Chemistry Volume-I For Class XII P591
- [50] Boyd L. O'Dell, Roger A. Sunde Boyd L. O'Dell, Handbook of Nutritionally Essential Mineral Elements 1997 p 495
- [51] Krivovichev, S. V., Filatov, S. K., & Cherepansky, P. N. (2009). The crystal structure of alumoklyuchevskite, K₃Cu₃AlO₂(SO₄)₄. *Geology of Ore Deposits*, 51(7), 656-662.
- [52] von Blanckenhagen, B., Tonova, D., & Ullmann, J. (2002). Application of the Tauc-Lorentz formulation to the interband absorption of optical coating materials. *Applied optics*, 41(16), 3137-3141.
- [53] POLITANO, A., et al. Indium selenide: an insight into electronic band structure and surface excitations. *Scientific reports*, 2017, 7.1: 3445.

- [54] Qasrawi, A. F. (2005). Dispersive optical constants and temperature-dependent band gap of cadmium-doped indium selenide thin films. *Semiconductor science and technology*.(20)8,765
- [55] Zhang, S. B., Wei, S. H., & Zunger, A. (2001). Intrinsic n-type versus p-type doping asymmetry and the defect physics of ZnO. *Physical Review B*, 63(7), 075205.
- [56] F. J. Manjón, A. Segura, V. Muñoz, G. Tobias, P. Ordejón, E. Canadell, *Phys. Rev. B* 2004, 70, 125201.
- [57] *Electron Spectroscopies Applied to Low-Dimensional Structures* (Eds: H. P. Hughes, H. I. Starnberg), Kluwer Academic Publishers, NY, 2002, pp. 382 – 390.
- [58] Terry, D. J., Zólyomi, V., Hamer, M., Tyurnina, A. V., Hopkinson, D. G., Rakowski, A. M. & Novoselov, K. (2018). Infrared-to-violet tunable optical activity in atomic films of GaSe, InSe, and their heterostructures. *2D Materials*, 5(4), 041009.
- [59] Feng, Wei, et al. "Back gated multilayer InSe transistors with enhanced carrier mobilities via the suppression of carrier scattering from a dielectric interface." *Advanced Materials* 26.38 (2014): 6587-6593.
- [60] O. Madelung, *Semiconductors: data handbook*. (Springer Science & Business Media, New York, (2012)).
- [61] Pannipitiya, Asanka, et al. "Improved transmission model for metal-dielectric-metal plasmonic waveguides with stub structure." *Optics express* 18.6 (2010): 6191-6204
- [62] Khusayfan, Najla M., and Hazem K. Khanfar. "Design and performance of (Au, Yb)/ZnS/InSe/C heterojunctions as plasmon resonators, photodetectors and microwave cavities." *Journal of Electronic Materials* 46, no. 3 (2017): 1650-1657.
- [63] Nelson, P. Issac, R. Arthi, R. Rathes Kannan, T. PonmudiSelvan, E. Ajitha, A. Ashina, and B. Vidhya. "Influence of heat treatment on the properties of thermally evaporated copper selenide thin films." *Materials Letters* 223 (2018): 14-16.
- [64] Khusayfan, Najla M., and Hazem K. Khanfar. "Design and performance of (Au, Yb)/ZnS/InSe/C heterojunctions as plasmon resonators, photodetectors and microwave cavities." *Journal of Electronic Materials* 46, no. 3 (2017): 1650-1657.
- [65] Pannipitiya, Asanka, et al. "Improved transmission model for metal-dielectric-metal plasmonic waveguides with stub structure." *Optics express* 18.6 (2010): 6191-6204
- [66] Alharbi, S. R., and A. F. Qasrawi. "Plasmon-electron dynamics at the Au/InSe and Y/InSe interfaces designed as dual gigahertz-terahertz filters." *Optik* 136 (2017): 524.

الملخص

في هذه الأطروحة، قمنا بدراسة مدى تحسين الأداء البصري والعازلية لرقائق InSe من خلال تطعيمها بعنصر النحاس، تمت دراسة الرقائق التي تم تحضيرها بواسطة تقنية التبخير الحراري تحت ضغط جوي 10^{-5} ميلي بار بنائياً وضوئياً من خلال تقنية حيود الأشعة السينية وقياس الطيف الضوئي. تم فحص نسبة التطعيم في العينات من خلال تقنية تشتت الأشعة السينية وكانت النتيجة بنسب 0%، 3%، 1.5%. وقد لوحظ أن الطبيعة العشوائية لرقائق InSe لم تتغير في هذا المستوى من التطعيم. ومع ذلك، فإن القياسات البصرية كشفت عن قيم فجوات الطاقة والتي بلغت 1.38 إلكترون فولت لرقائق InSe غير المطعمة. إن التطعيم بنسبة 3% أدى إلى زيادة قيمة فجوة الطاقة بنسبة 29% وتقليل عرض مستويات الطاقة الممتدة InSe بنسبة 76%، مما يشير إلى تحسن الاستجابة البصرية. بالإضافة إلى ذلك، فإن التطعيم بنسبة 1.5% زاد من خصائص العازلية والتوصيل. وتبين أيضاً أن ثابت العزل الكهربائي عند مستوى الرنين يزداد من 12 إلى 15 وأن سرعة الانجراف لكل وحدة مجال كهربائي ازادت من 45 إلى 55 سم²/فولت. ثانياً مع زيادة نسبة التطعيم.